

Identification Method of Tire-Road Adhesion Coefficient Based on Tire Physical Model and Strain Signal for Pure Longitudinal Slip

Jintao Zhang – Zhecheng Jing – Haichao Zhou ✉ – Yu Zhang – Guolin Wang

Jiangsu University, School of Automotive and Traffic Engineering, China

✉ hczhou@ujs.edu.cn

Abstract To precisely calculate the tire-road adhesion coefficient of rolling tires at various slip rates, and enhance the safety and stability of vehicle operation, an approach for estimating the tire-road adhesion coefficient based on strain sensors and brush models was proposed. First, a finite element model of 205/55R16 radial tire was established, and the effectiveness of the model was verified through static ground contact and radial stiffness experiments. Then, the circumferential strain signal of the inner liner centerline of the tire during braking was extracted, utilizing the average peak angle spacing of the first-order and second-order circumferential strain curves, and the contact area length was estimated using the arc length formula. Subsequently, the braking simulation of rolling tires confirmed the asymmetry of pressure distribution within the ground contact area, estimating the position of slip points within the contact area based on arbitrary pressure distribution function and brush model, while nonlinear regression was utilized to fit the estimation function of slip point under various slip rates. Finally, a functional relationship was developed between tire-road adhesion coefficient and slip rate, considering the friction characteristics between tire rubber and road surface, while the friction model is based on exponential decay. The results suggest that the methods described above enable estimation of the tire-road adhesion coefficient under different slip rates, providing valuable insights for intelligent tire applications in vehicle dynamics control.

Keywords intelligent tire, tire-road adhesion coefficient estimation, slip point, slip rate, nonlinear regression

Highlights

- Estimated ground contact mark length using strain signals from the tire's inner liner.
- Analyzed pressure distribution in tire contact areas under pure longitudinal slip.
- Estimated slip points in contact areas and derived a function for various slip rates.
- Created a function to estimate road adhesion under slip with successful validation.

1 INTRODUCTION

The tire is the only part of the vehicle in contact with the road surface, transmitting the forces and torques required to move the vehicle. Therefore, it is important to accurately obtain the adhesion coefficient between the tire and the road surface during vehicle driving to improve the braking performance, driving smoothness, and handling stability of the vehicle [1,2]. At the same time, as one of the key components of the vehicle dynamics control system, the tire plays a "passive" role in vehicle dynamics control. The adhesion coefficient between the tire and the road surface cannot be directly obtained. With the continuous development of vehicle intelligence, the concept of the intelligent tire was proposed by installing sensors inside the tire to make the tire an 'active' component in vehicle dynamics control and to obtain contact information between the tire and the road surface directly [3]. At present, most researchers' methods of estimating tire-road adhesion coefficient through intelligent tires are mainly divided into experiment-based methods and model-based methods.

In estimating the tire-road adhesion coefficient through experiment-based methods, most researchers try to measure the parameters related to friction between tire and road, such as tire noise, longitudinal and lateral tire deformation, and find the correlation between the sensor signal characteristics and the tire-road adhesion coefficient. Alonso et al. [4] utilized the different noise levels of cars driving on roads with different adhesion conditions to build a system architecture and signal processing algorithm for measuring noise, which was used to measure road adhesion conditions. Some other researchers estimate road conditions by using microphones to

record distinct noise data vehicles generate as they traverse different roads [5,6]. Kuno et al. [7] studied a real-time monitoring method for asphalt pavement conditions based on charge-coupled device (CCD) cameras, using average absolute deviation and reference brightness signals to detect the glossiness of the pavement, determine the pavement condition, and improve the accuracy of vehicle avoidance control systems. Xu et al. [8] designed an intelligent tire system by installing a three-axis acceleration sensor in the center of the tire lining layer to extract the three-direction acceleration signal of the tire and analyze the characteristic parameters of the circumferential acceleration. Using the support vector machine algorithm, this approach can classify and recognize different road surfaces. Estimation of tire-road adhesion coefficients through experiment-based method is relatively demanding. Since the sensor needs to be installed inside the tire, the signal is easily interfered by external noise during vehicle driving and faces problems such as sensor power supply and high price [9]. At the same time, a large amount of signal data needs to be tested for signal characterization and feature extraction as training samples for artificial intelligence algorithms such as neural networks. Although the accuracy of the estimation is high, once it deviates from the training conditions, the accuracy of the estimation is greatly reduced. Usually, the estimated tire-road adhesion coefficient is a constant value and does not describe the process of tire-road adhesion coefficient variation with tire slip rate [10].

In model-based research, most researchers attempted to use simplified mathematical models to determine the adhesion coefficient

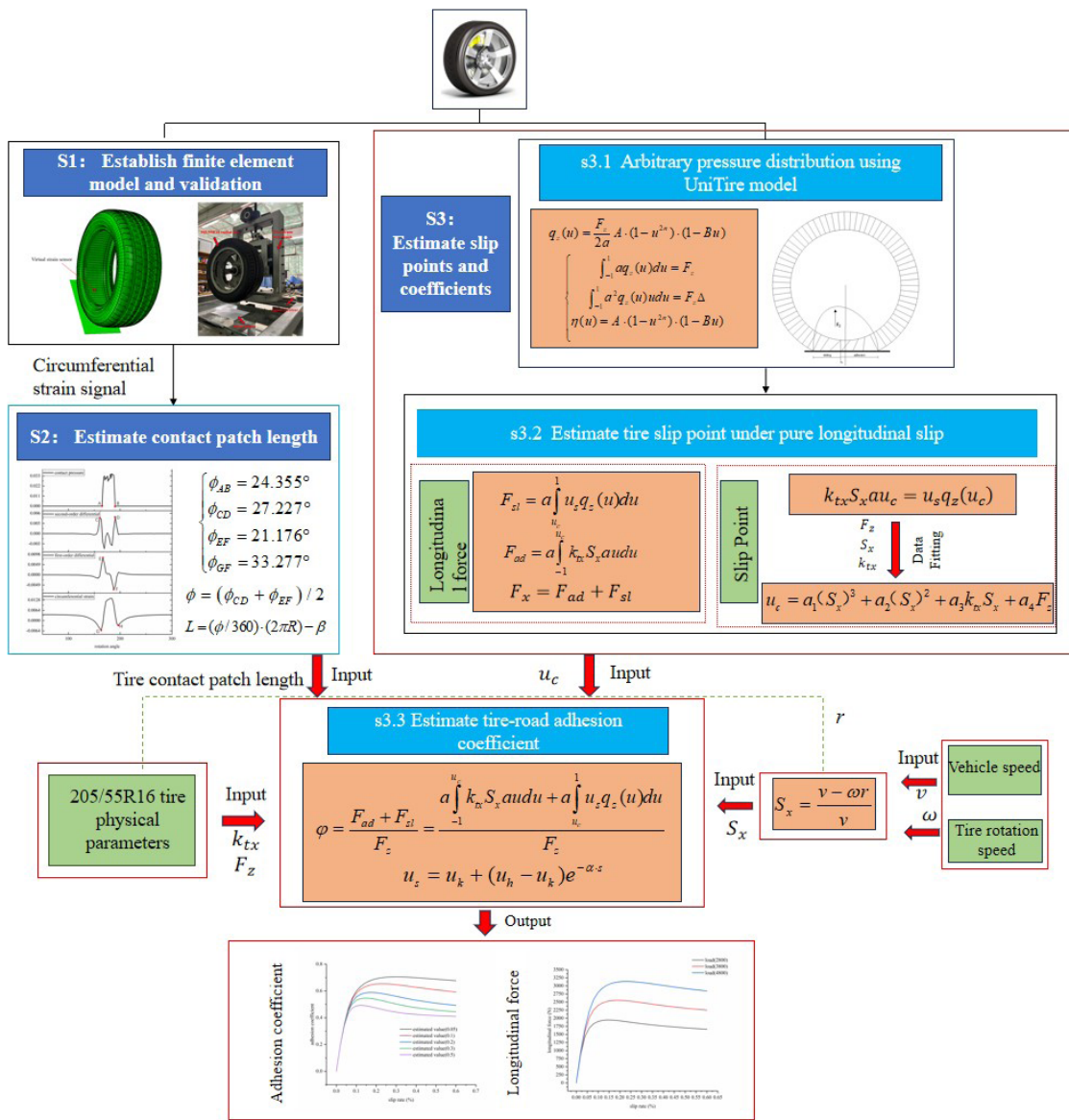


Fig. 1. Flowchart for identifying tire-road adhesion coefficient

between tire and road. There are three main types of mathematical methods used for this purpose: the vehicle dynamics model, the glide-based method, and the tire model. Matsuzaki et al [11] installed an acceleration sensor on the tire lining to extract the acceleration signal. They obtained deformation information and tire force in the tire connection area by integrating the signal. Finally, the obtained data parameters are plugged into the adhesion coefficient calculation formula, which is derived from the tire brush theory model, to estimate the tire-road adhesion coefficient. Rajamani et al. [12] delve into developing an independent friction coefficient estimation algorithm for each vehicle wheel. Three distinct parameters are formulated to estimate slip ratio and longitudinal tire force. Subsequently, a recursive least squares parametric formula is employed to estimate the friction coefficient. Nishihara et al. [13] defined the concept of grip margin using the brush model and friction circle theory, re-derived and analyzed the brush model theory, and completed the estimation of the tire-road adhesion coefficient. However, the pressure distribution of the brush model used was a quadratic parabolic distribution. The model-based method avoids the need for extensive experiments or simulations for data collection and is more generalizable than the

training models of intelligent algorithms such as neural networks. However, in the model-based method, the estimation of the tire-road adhesion coefficient often requires an accurate mathematical model to describe the mechanical characteristics of the tire-road contact, such as the contact pressure distribution. At the same time, in the process of constructing the algorithm, the issue of necessary grounding parameter inputs is sometimes overlooked because of the limitations of the on-board sensors, which do not allow real-time access to certain feature parameters.

In summary, the goal is to improve the vehicle's drive braking performance under purely longitudinal slip conditions and promote the development of intelligent chassis technology. This paper designs a method for estimating the tire-road adhesion coefficient at different slip rates by combining the sensor signals with a mathematical model of the tire, used to calculate the optimum slip rate and peak adhesion coefficient of a tire, as shown in Fig. 1. First, the finite element model of a passenger car tire 205/55R16 was established, and it is validated using the contact sizes and radial stiffness in S1. Second, based on the circumferential strain signal characteristics of the centerline of the inner liner of the rolling tire, the estimation methods

for contact angle and contact area length were designed in S2. In S3, synthetic application of a tire arbitrary pressure distribution function, pure longitudinal slip model, and a computing method for the tire-road adhesion coefficient are proposed. To complete the computing method, the S3 includes three substeps: an arbitrary pressure distribution function based on the UniTire model is introduced to reflect the rolling tire contact pressure in the substep of S3.1. Then, with the help of the theoretical analysis of the pure longitudinal slip brush model, the calculation methods for tire longitudinal force and slip point position are put forward in the substep S3.2. Finally, in S3.3, according to the friction theorem, and taken tire physical parameters and vehicle speed into consideration, the estimation function of the tire-road adhesion coefficient under different slip rates is built. Estimations of the tire-road adhesion coefficients under different slip rates of rolling tire are also achieved.

2 METHODS & MATERIALS

2.1 Tire Model

Simplifications and assumptions were employed in the development of the finite element model of the passenger car tire 205/55R16. These are deemed less influential in terms of simulation precision and are outlined as follows:

1. To facilitate computations, define a two-dimensional plane as a rigid surface body for simulating the road surface.
2. Ignore the influence of temperature during tire rolling.
3. Ignore the effects of road surface roughness.

A tire is not made of a single rubber material but various materials with relatively complex structure. Therefore, a finite element model is established, which is divided into structural and tread pattern models [14]. First, the 205/55R16 tire was cut in the laboratory to obtain the cross-sectional structure of the tire. A two dimensional (2D) axisymmetric structure model was established based on the actual tire structure profile and material distribution, in which the rubber element types are CGAX3H and CGAX4H, and the reinforcing materials, such as the carcass and belts, are established by the SFMGA1 plane element. The rubber solid element is embedded with rebar elements to simulate the features of the tire cord rubber composite material. The geometric parameters of the reference tread pattern blocks are used to import a 2D cross-section tire model into ABAQUS software. The 2D cross-section tire model is rotated to create a 3D solid mesh model as shown in Fig. 2.

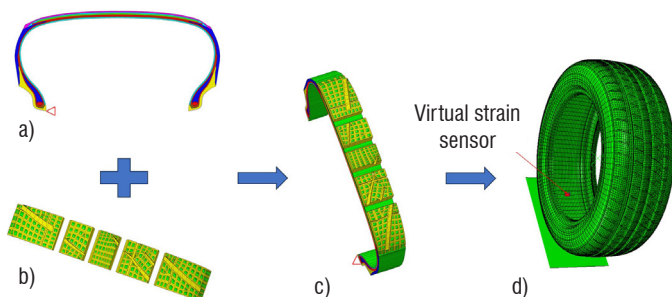


Fig. 2. Finite element model for the passenger car tire 205/55R16;

a) 2D cross-section tire model, b) tread pattern block, c) one tire patch, and d) 3D tire model

The single-pitch 3D tread pattern solid model is established using the CATIA software and imported into the HYPERMESH software to generate the 3D mesh. Considering the incompressibility of rubber materials, the corresponding grid type is the hybrid element C3D8RH [15]. The 3D tire model, including the complex tread pattern, is shown in Fig. 2d with 123842 elements and 155703 nodes.

We specified the contact properties between the tire tread and road as hard contact and model the variation of the friction coefficient between the tire tread and road with slip speed using the Coulomb friction model.

The tire's rubber material exhibits typical viscoelastic, incompressible, and doubly nonlinear characteristics of both material and geometry. The accuracy of the material model significantly impacts the analysis's convergence during tire dynamic performance. Building upon our team's prior research [16,17], the Yeoh model represents the rubber material and is defined as:

$$W = c_1(I_1 - 3) + c_2(I_1 - 3)^2 + c_3(I_1 - 3)^3, \quad (1)$$

where W is strain energy density, in which c_1, c_2, c_3 are material constants and I_1 is the first strain invariant.

$$I_1 = \lambda_1^2 + \lambda_2^2 + \lambda_3^2 = \text{tr}(\mathbf{C}), \quad (2)$$

where $\lambda_i (i=1,2,3)$ are stretch ratios and the square root of the right Cauchy-Green strain tensor (\mathbf{C}).

The selection of intelligent tire sensors mainly includes three-axis accelerometers, strain sensors, optical sensors, and others. Strain sensors offer advantages such as high precision, wide measurement range, fast response, durability, reliability, and ease of installation and integration. Compared to accelerometers, the signals from strain sensors are less susceptible to interference from tire noise. Based on the previous research conducted by the research team on the force-sensitive response regions of tires, it was found that under braking conditions, the deformation caused by the contact between the tire and the ground primarily occurs at the tread. Therefore, circumferential strain signals were extracted and analyzed by comparing the strain at the tread and the inner liner centerline, as shown in Fig. 3. The tread pattern significantly influences the circumferential strain signal at the tread centerline, resulting in large fluctuations in the signal, which are particularly evident at the signal's troughs. These fluctuations hinder the effective extraction of sensitive signal features.

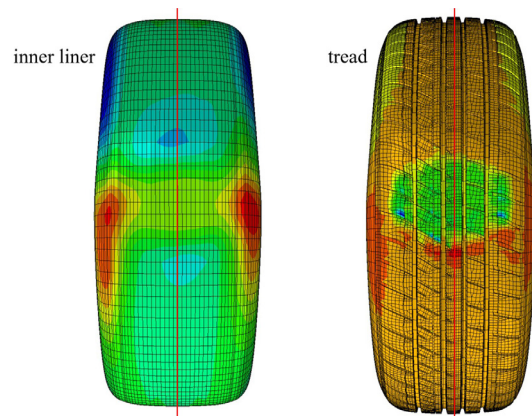


Fig. 3. Strain signal extraction locations

Compared to the circumferential strain signal at the tread centerline, the strain signal at the inner liner centerline is less affected by the tread pattern as seen in Fig. 4. The signal curve is smoother and more stable, with its trend opposing the tread centerline strain signal. This discrepancy is primarily related to the tire's structure, material properties, and load distribution. When the tire is subjected to external loads and in contact with the ground, the tread experiences compression and elongation due to frictional forces, resulting in significant localized deformation. The tire structure is multi-layered and composite, and due to the differing elastic moduli and response characteristics between the tread and the inner liner, the inner liner undergoes deformation that is opposite to that of the tread. Therefore,

by extracting the circumferential strain signal of the point in the inner liner centerline under the rolling tire braking condition, the signal is selected to represent the real-time strain sensor signal of the rolling tire. The specific location of this point is shown in Fig. 2d.

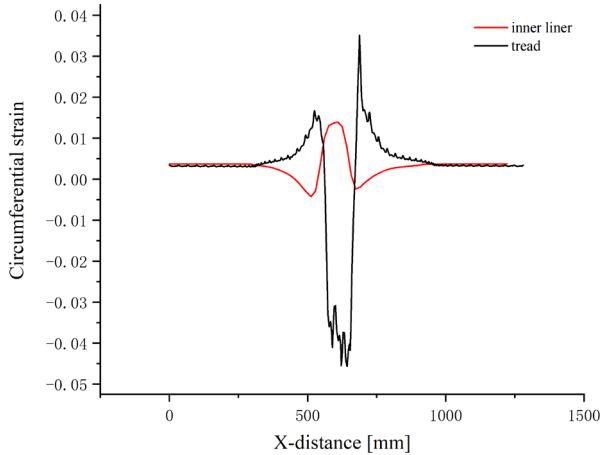


Fig. 4. Comparison of circumferential strain signals between tread and inner liner

2.2 Experimental Verification

To verify the accuracy of the tire finite element model established, the results were verified using the tire static ground contact distribution characteristics test and tire radial stiffness test. A static ground contact test was performed using a tire drum testing machine; during the test, the tire was loaded to a rated load of 3800 N, and the inflation pressure was set to 210 kPa. The ground contact area of the tire under static loading is obtained through red ink printing, and the ground contact geometric parameters are extracted, as shown in Figs. 5 and 6.



Fig. 5. Tire stiffness test benchP

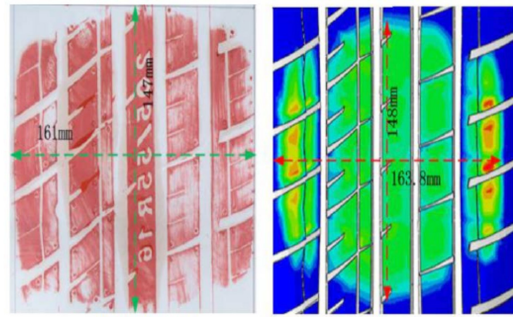


Fig. 6. Comparison of the sizes of tire contact area

Table 1. The tire ground contact characteristics

Title	Experiment values [mm]	Simulate values [mm]	Error [%]
Contact width	147	148	0.67
Contact length	161	163.8	1.74

Table 1 shows that the error between the tire contact geometric properties obtained by finite element simulation and the test result is less than 2 %, indicating that the tire finite element model established in this paper can accurately describe the tire ground contact characteristics.

To further verify the accuracy of the tire finite element model, a comprehensive strength testing machine was used to conduct tire radial stiffness tests. The test and simulation results of tire sinkage and static loading radius under different test conditions are shown in Table 2, and the test and simulation results of radial stiffness are shown in Fig. 7. It can be seen from the Table 2 and Fig. 7 that the tire sinkage, static loading radius, and radial stiffness of the test and simulation are consistent.

2.3 Estimate Contact Patch Length

According to the simulation results of the circumferential strain signals of the liner centerline and tread centerline of rolling tire [18], this paper introduces a virtual strain sensor that utilizes strain information from a node on the longitudinal centerline of the tire inner liner, as illustrated in Fig. 2d. When the tire is subject to the 8 % slip rate, a 3800 N load, and 0.21 MPa inflation pressure, the circumferential strain signal of the tire inner liner centerline during braking is obtained through the virtual strain sensor. The ground pressure signal at the centerline of the tire's inner liner is obtained and analyzed. The results are shown in Fig. 8.

$$\begin{cases} \phi_{QP} = 24.355^\circ \\ \phi_{CD} = 27.227^\circ \\ \phi_{EF} = 21.176^\circ \\ \phi_{GH} = 33.277^\circ \end{cases} \quad (3)$$

where ϕ_{QP} is actual rolling tire contact angle, ϕ_{CD} is the peak angle spacing of the second-order, ϕ_{EF} is the peak angle spacing of the first-order, ϕ_{GH} is the peak spacing of the circumferential strain.

Table 2. Comparison of test and simulation results of tire sinkage and static loading radius

Test conditions	Experiment values				Simulation values			
	210 kPa		250 kPa		210 kPa		250 kPa	
/	Sinkage [mm]	Static radius [mm]	Sinkage [mm]	Static radius [mm]	Sinkage [mm]	Static radius [mm]	Sinkage [mm]	Static radius [mm]
123 kg	6.01	308.14	5.49	309.01	6.48	309.47	5.98	309.97
246 kg	12.28	301.87	11.13	303.37	12.17	303.78	11.62	304.33
369 kg	18.06	296.09	16.29	298.21	18.28	297.67	16.99	298.96

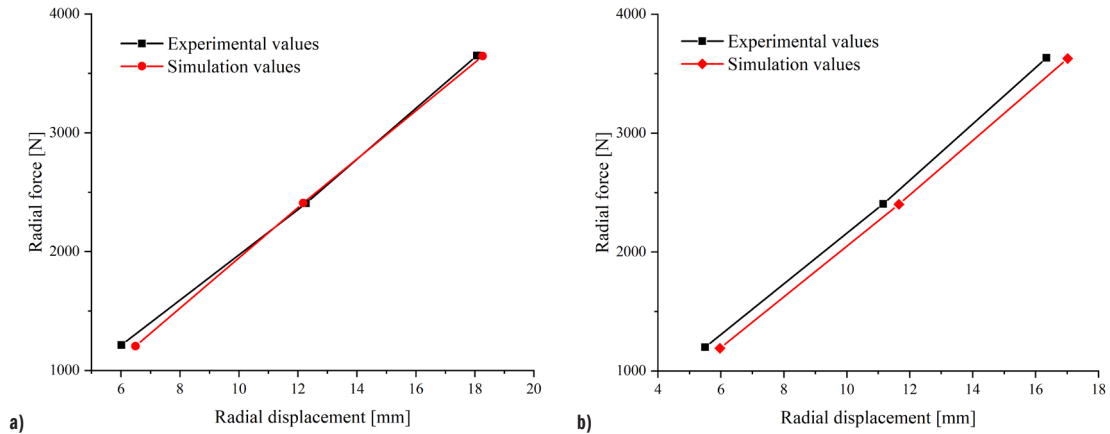


Fig. 7. Comparison of tire radial stiffness under different inflation pressure; a) 210 kPa, and b) 250 kPa

ϕ_{QP} is the actual rolling tire contact angle. It can be obtained that the difference between the rolling tire contact angle and the peak angle spacing of the first-order and second-order derivative curves of the circumferential strain is about 3° , and the difference with the peak angle spacing of the circumferential strain signal is about 10° . Therefore, the rolling tire contact angle can be estimated by averaging the circumferential strain signal's first- and second-order peak pitch angles, as shown in Eq. (4).

$$\phi = (\phi_{CD} + \phi_{EF}) / 2, \tag{4}$$

where ϕ is estimated contact angle.

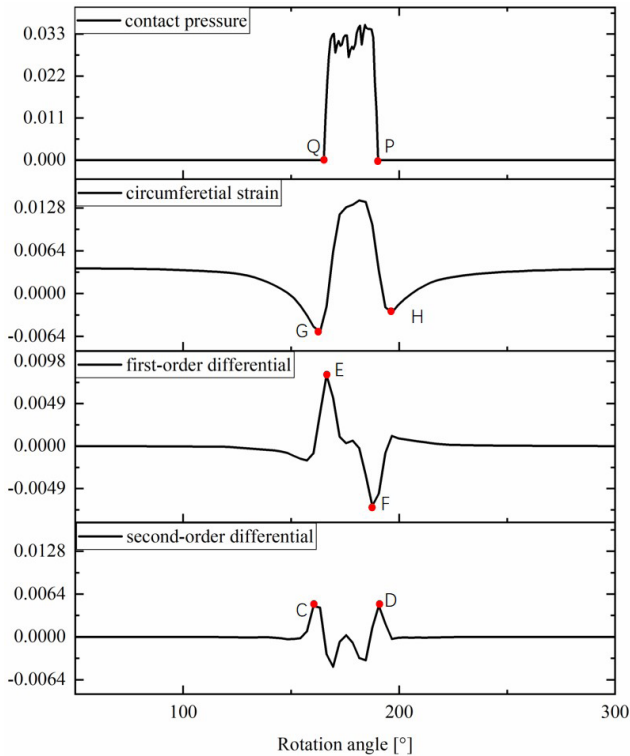


Fig. 8. Comparison between peak angle difference of circumferential strain of tire inner liner and contact angle

To investigate the influence of rolling tires on the tire contact angle during braking, we conducted simulation analysis of pure longitudinal slip conditions under free rolling and slip rates of 2 %, 4 %, 6 %, 8 %, and 10 %, with load of 3800 N and inflation pressure of 0.21 MPa. Figure 9 shows the simulation results. During free-rolling,

the front and rear contact angles are equal. When the tire begins to slip, the position of the midpoint of the tread in the finite element simulation starts to move toward the front. As the slip ratio increases, the front contact angle increases while the rear contact angle decreases, increasing the asymmetry of the contact angles. When the tire is in a high slip ratio, the trend of increasing contact angle asymmetry slows down, consistent with the results in [19]. Therefore, when estimating the tire's contact area length during braking based on the contact angles, the assumption of equal front and rear contact angles should not be used. Instead of using trigonometric functions, the arc length formula does not require distinguishing between the magnitudes of the front and rear contact angles. This makes it more suitable for estimating the contact area length of a rolling tire during the braking process. The formula for estimating the contact area length is given by Eq. (5)

$$L = (\phi / 360) \cdot (2\pi R), \tag{5}$$

where L is estimated contact area length.

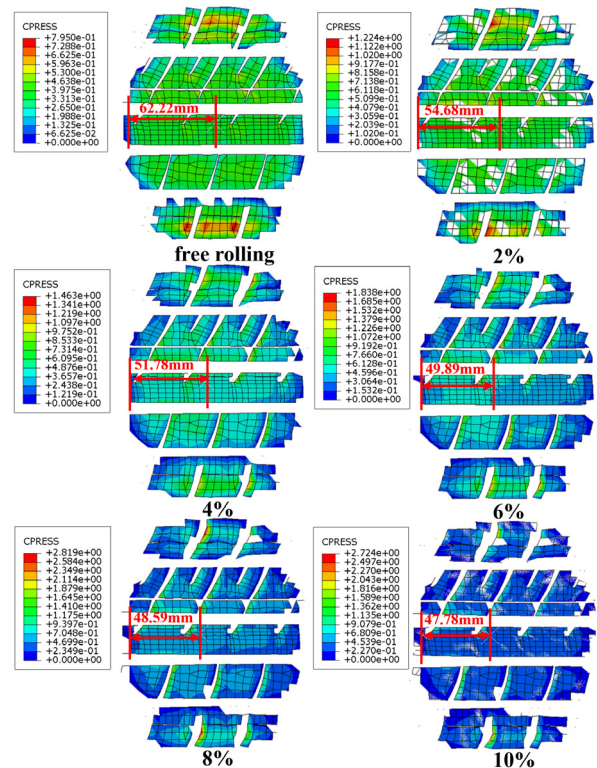


Fig. 9. Comparison of asymmetric contact angles

Figure 10 shows a rolling tire's estimated contact area length under different loads, compared with the contact area length obtained from finite element simulation. It can be observed that since the arc length is greater than the straight-line length, the estimated contact area length is larger than the simulation result, with a relative error exceeding 6 %. Under low and high load conditions, the error between the estimated and simulated values is minor, and it becomes larger under moderate load. To reduce the error in the estimated contact area length, a correction factor β accounts for the length difference between the arc and the straight line, as shown in Eq. (6).

$$L = (\phi / 360) \cdot (2\pi R) - \beta. \quad (6)$$

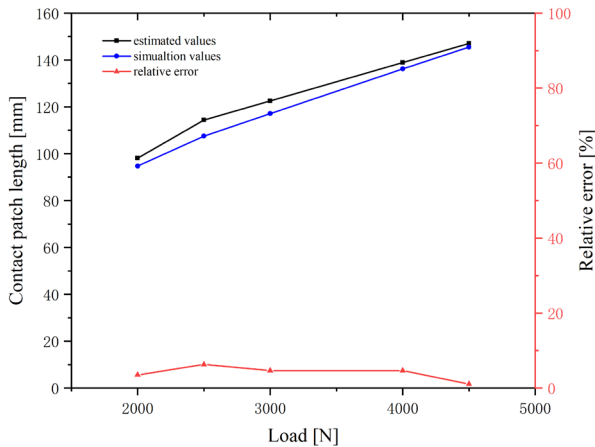


Fig. 10 Estimation and simulation values of contact area length under different loads

To determine the value of the correction factor β , values of β were chosen as 1 mm, 2 mm, 3 mm, and 4 mm to calculate the relative error in the contact area length for each correction factor, as shown in Fig. 11. It can be observed that as the value of β increases, the estimation accuracy of the contact area length improves. After considering the overall performance for different values of β , a correction factor β of 3 mm was selected.

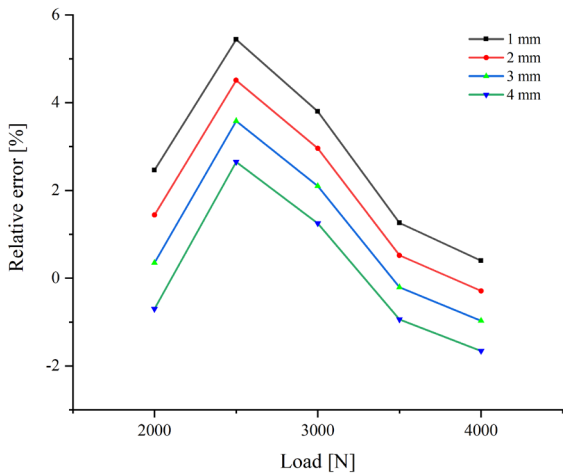


Fig. 11. Relative error of different correction factor values

Simulation results were further used to obtain ϕ_1 of the grounding angle and L_1 of the contact area length under different loads. Estimated values for the contact angle ϕ_2 and the contact area length L_2 are determined using Eqs. (4) and (6). Comparison shown in Fig. 12 reveals that the disparity between simulated value ϕ_1 and estimated value ϕ_2 of the contact angle is less than 1° , and the maximum error between simulated value L_1 and estimated value L_2 of the contact

area length does not exceed 3 mm, verifying the accuracy of this estimation method.

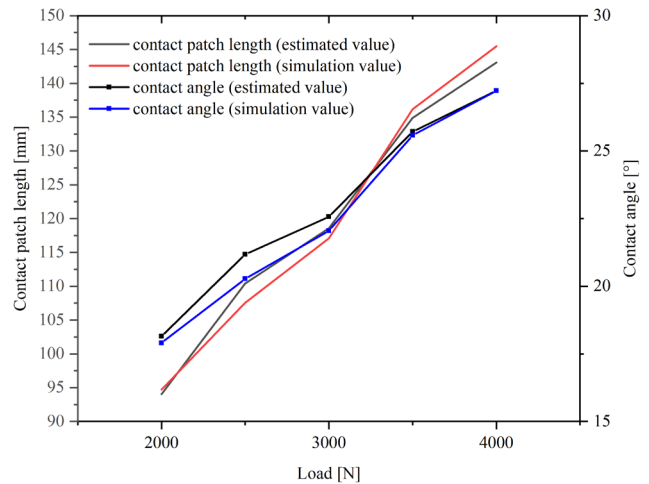


Fig. 12. Comparison of contact parameter estimation results under different loads

3 RESULTS AND DISCUSSION

3.1 Contact Pressure Distribution of Rolling Tires

Accurately describing the pressure distribution within the tire's contact area is crucial for ensuring the accuracy of estimates concerning longitudinal forces, slip point, and tire-road adhesion coefficients. Typically, pressure distribution within the tire's contact area is assumed to follow a symmetrical parabolic distribution. However, this symmetrical parabolic distribution only applies when the tire is in a state of free rolling within small loads. Under varying working conditions, a symmetrical parabolic distribution cannot accurately represent actual tires. Hence, according to the tire contact pressure distribution function presented in UniTire model [20], this article utilizes arbitrary pressure distribution within the UniTire model to uniformly express the pressure distribution of rolling tires during braking. The pressure distribution of the tire is defined as follows:

$$q_z(u) = \frac{F_z}{2a} A \cdot (1 - u^{2n}) \cdot (1 - Bu), \quad (7)$$

where F_z is the vertical load, a is the half-length of the contact area, and A, B are undetermined coefficients.

The vertical load offset of the tire is set to Δ . According to the mechanical characteristics of the tire, the relationship between contact pressure distribution and tire vertical load F_z needs to be satisfied:

$$\begin{cases} \int_{-1}^1 a q_z(u) du = F_z \\ \int_{-1}^1 a^2 q_z(u) u du = F_z \Delta \\ \eta(u) = A \cdot (1 - u^{2n}) \cdot (1 - Bu) \end{cases}, \quad (8)$$

while the following boundary conditions should be met:

$$\begin{cases} \eta(1) = \eta(-1) = 0 \\ \eta(u) \geq 0, u \in [-1, 1] \\ \eta(u) = 0, u \notin [-1, 1] \\ \int_{-1}^1 \eta(u) du = 2 \\ \int_{-1}^1 \eta(u) \cdot u \cdot du = 2 \cdot \frac{\Delta}{a} \end{cases}. \quad (9)$$

According to the boundary conditions the expression of A and B can be defined as:

$$\begin{cases} A = \frac{2n+1}{2n} \\ B = -\frac{3 \cdot (2n+3)}{2n+1} \cdot \frac{\Delta}{a} \end{cases} \quad (10)$$

The influence of n and Δ/a on the contact pressure distribution function is shown in Fig. 13. The parameter n significantly influences the uniformity of pressure distribution, while parameter Δ/a mainly affects the peak distribution on either side of the tire.

Table 3. Simulation schemes

Number	Load [N]	Inflation pressure [MPa]	Friction coefficient
1	2800	0.21	0.5
2	3800	0.21	0.5
3	4800	0.21	0.5
4	3800	0.26	0.5
5	3800	0.31	0.5
6	3800	0.21	0.1
7	3800	0.21	0.9

To verify the contact pressure distribution characteristics of a rolling tire during braking, it is necessary to determine the values of the parameters for the arbitrary pressure distribution function and assess whether this function can accurately describe the contact pressure distribution between the tire and the ground during braking. We designed seven different finite element simulation schemes using the control variable method to determine the effect of load, inflation pressure, and longitudinal force on pressure distribution under free rolling and braking conditions. The details of each simulation scheme are shown in Table 3.

Figure 14 illustrates the pressure distribution within the contact area of rolling tires under varying loads. The tire inflation pressure is 0.21 MPa, the speed is 70 km/h, the friction coefficient is 0.5, and the slip rate of rolling tires during braking is 8%. For the convenience of research, the pressure distribution simulation result is obtained by extracting the longitudinal centerline of the tire contact area. As shown in Fig. 14a, as the weight on a tire increases or decreases, and the length of its contact area with the ground also changes. When the tire bears more weight, the contact area becomes longer due to radial deformation of the tire. This happens because the tire deforms radially when subjected to greater loads. Additionally, as the weight increases, the highest-pressure point in the center of the

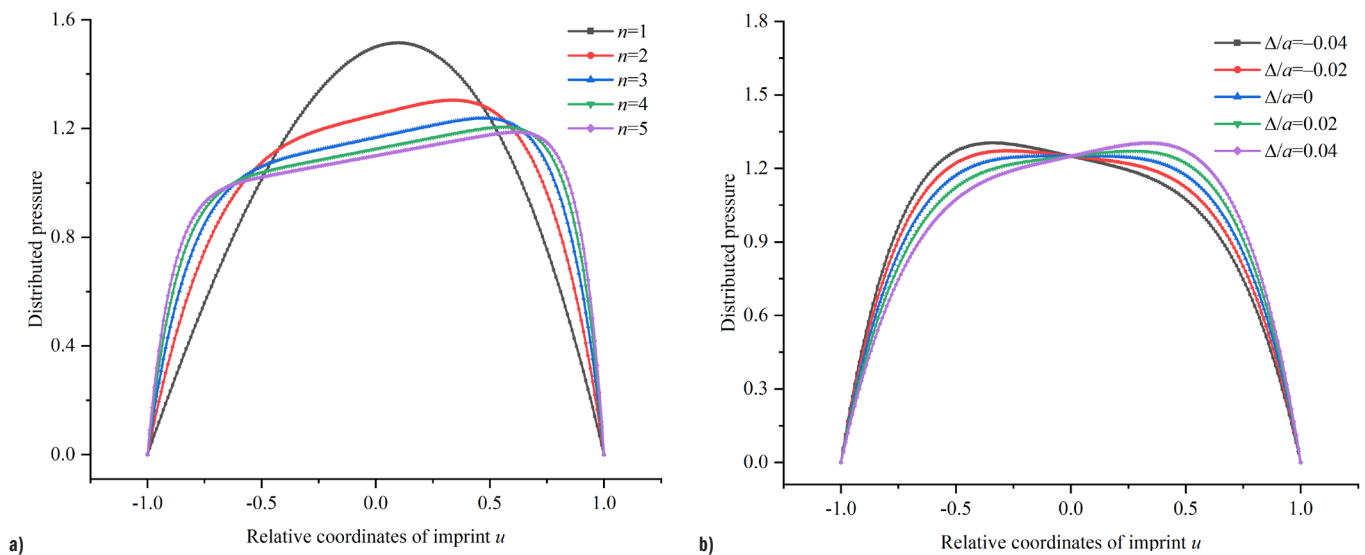


Fig. 13. Arbitrary pressure distribution with different parameters; a) $\Delta/a = 0.04$, $n = 1, 2, 3, 4, 5$, and b) $n = 2$, $\Delta/a = -0.04, -0.02, 0, 0.02, 0.04$

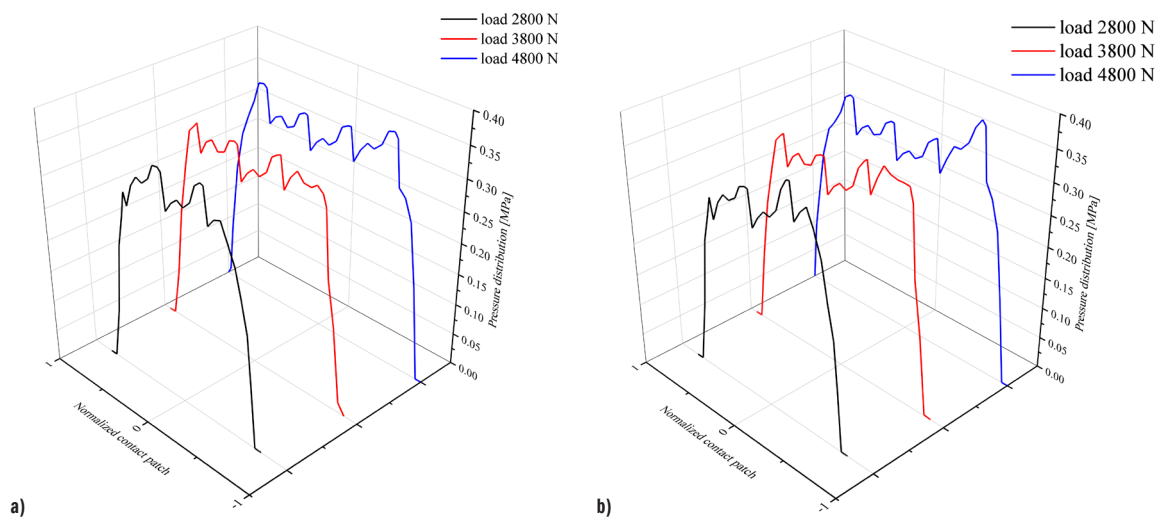


Fig. 14. Comparison of contact pressure distribution under the different loads: a) free rolling; b) braking

tire's contact area decreases while the highest pressure on both sides increases. Similar simulation results are obtained under braking conditions, as shown in Fig. 14b. The comparison of contact pressure between the free rolling and the braking conditions shows that pressure distribution is approximately symmetric in free rolling but asymmetric in braking conditions.

Figure 15 illustrates the pressure distribution within the contact area of rolling tires under varying inflation pressure; the tire load is 3800 N, the speed is 70 km/h, the friction coefficient is 0.5, and the slip rate of rolling tires during braking is 8 %. Figure 15a indicates that when the inflation pressure is 0.31 MPa, the contact area length of the rolling tires is less than that of 0.21 MPa. The tire's overall stiffness changes with the inflation pressure when the load remains unchanged. The higher the tire's inflation pressure, the less it deforms against the ground and the smaller the ground contact area becomes. Similar results are obtained under braking conditions.

Figure 16 illustrates the pressure distribution within the contact area of rolling tires under varying friction coefficients; the tire inflation pressure is 0.21 MPa, the speed is 70 km/h, the load is 3800 N, and the slip rate of rolling tires during braking is 8 %. Figure 16a shows that under free rolling conditions, the peak value of tire contact pressure increases with the increase of friction coefficients. However, the increasing trend is relatively small, and the length of the tire contact area remains unchanged. In Figure 16b, it can be observed that under braking conditions with an 8 % slip ratio, the pressure distribution between the tire and the ground shifts toward the front.

Furthermore, as the road surface friction coefficient increases, the higher friction coefficient intensifies the frictional force between the tire and the ground, making the changes in the front end of the contact pressure distribution more pronounced.

Based on the finite element simulation results of contact pressure distribution under different operating conditions shown in Figs. 14-16, it is demonstrated that the contact pressure distribution during tire braking is not parabolic symmetrical. Instead, the pressure distribution shifts toward the front end of the contact area depending on changes in operating conditions. In Figure 13, the arbitrary pressure distribution function solved in MATLAB can be adjusted by changing the values of parameters, thereby modifying the shape of the pressure distribution. Therefore, to describe the forward shift in contact pressure distribution during braking, parameters are set to -0.04 and 2 , respectively, to approximate the characteristics of the contact pressure distribution between the rolling tire and the ground under braking conditions.

3.2 Estimate the Slip Point Based on Tire Brush Model

Under the condition of pure longitudinal slip, the tire only slips in the rolling direction, and the slip angle and lateral speed are zero, therefore, the linear speed of the tire is equal to the vehicle speed. During a vehicle's braking process, the tires undergo three phases: free-rolling, sliding while rolling, and pure slip, which is a dynamic and progressive process. Under braking conditions, a tire's slip rate

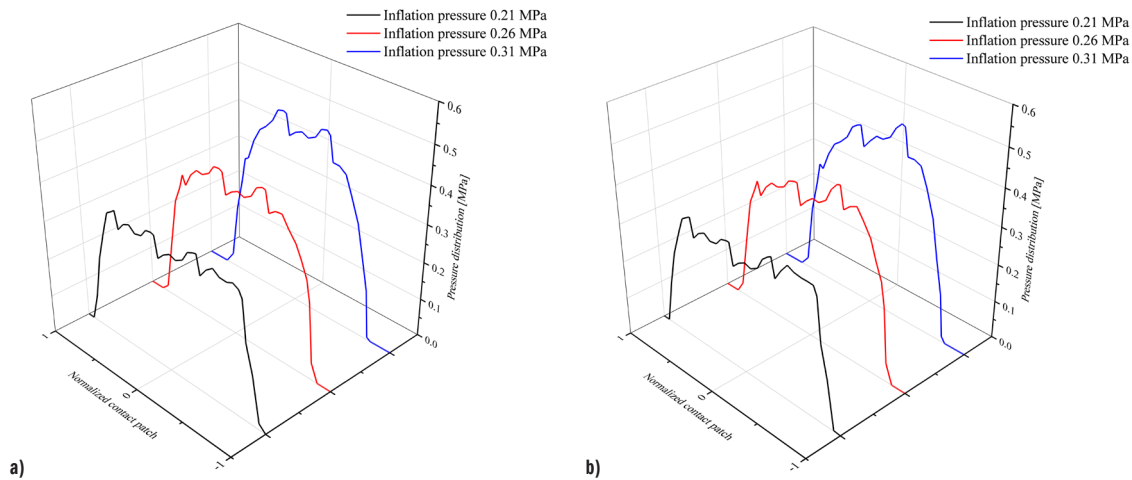


Fig. 15. Comparison of contact pressure distribution under the different inflation pressures; a) free rolling, and b) braking

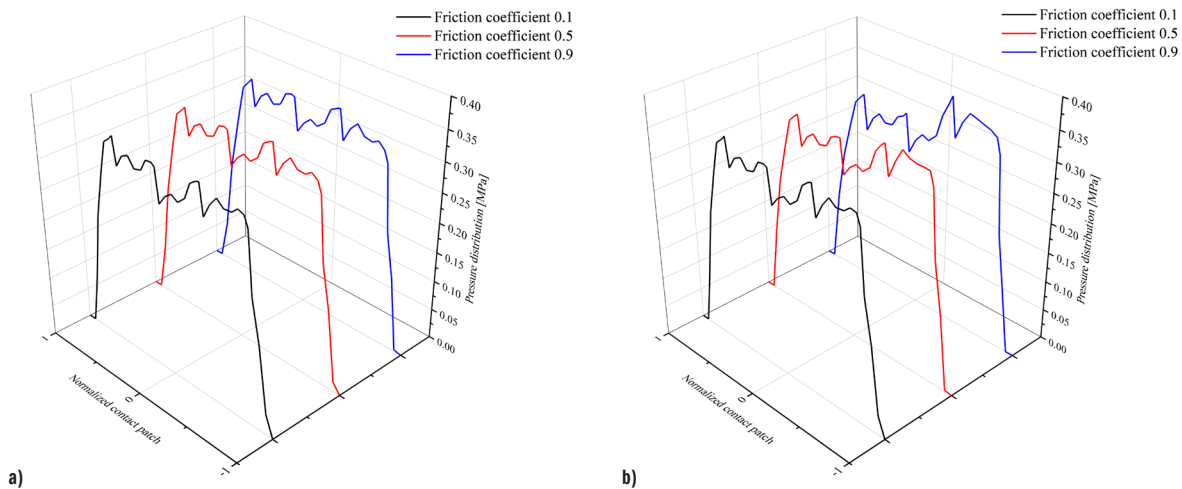


Fig. 16. Comparison of contact pressure distribution under the different friction coefficients; a) free rolling, and b) braking

is calculated from the linear and rolling tire angular velocities at a known effective rolling radius, which is defined as shown in Eq. (11).

$$S_x = \frac{v - \omega r}{v}, \quad (11)$$

where v and ω represent the vehicle speed and wheel angular speed respectively; r is the free-rolling radius of the wheel.

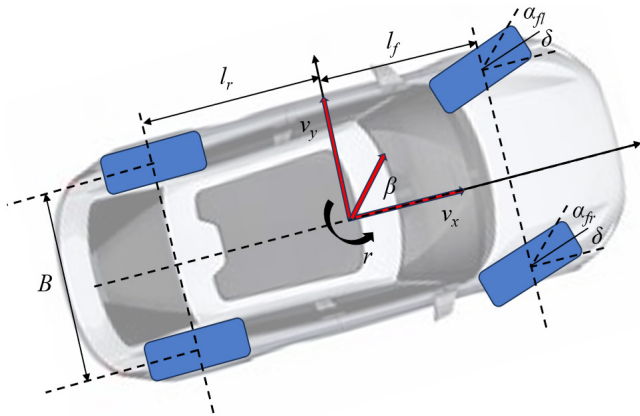


Fig. 17. Vehicle dynamics modeling

Accurate calculation of a tire's slip rate during vehicle braking requires accurate determination of the tire's linear and angular velocities as well as the size of the effective rolling radius. Wheel speed sensors on current vehicles can accurately measure the rolling tire's angular velocity while the vehicle is in motion, and the tire's linear velocity can be obtained from a body viewer or global positioning system (GPS). Several researchers have implemented the observation of longitudinal and transverse vehicle velocities using whole-vehicle dynamics models. However, the observed velocities represent the traveling speed at the vehicle's center. In order to study the relationship between the linear velocities of the four tires and the longitudinal and transverse velocities at the center of mass of the vehicle when the vehicle is moving, the relationship between the linear velocities of the four tires and the longitudinal and transverse velocities at the center of mass of the vehicle can be obtained by analyzing the whole vehicle's seven-degree-of-freedom dynamics model, which can be expressed as:

$$\begin{cases} v_{fl} = (v_x - \frac{B}{2}r)\cos\delta + (v_y + l_f r)\sin\delta \\ v_{fr} = (v_x + \frac{B}{2}r)\cos\delta + (v_y + l_f r)\sin\delta, \\ v_{rl} = v_x - \frac{B}{2}r, v_{rr} = v_x + \frac{B}{2}r \end{cases} \quad (12)$$

where v_{fl} , v_{fr} , v_{rl} , and v_{rr} denote the tire speeds of the left front wheel, right front wheel, left rear wheel, and right rear wheel, respectively; δ is the tire angle of rotation; B is the wheelbase between the tires of the vehicle; l_f and l_r denote the axle distances between the front and rear axles of the vehicle.

A uniform definition of the slip rate of a tire based on the update of the imprint coordinates is used in the Unitire tire model. Based on this idea, this paper expresses the bristle slip within the contact area by determining the slip rate at a point in the center of the contact area to simplify the description of the bristle slip at different parts.

The brush model is a basic physical representation of a tire. It simplifies the tire as a rigid ring connected to a set of bristles. This model assumes that the bristles undergo elastic deformation when the tire touches the ground and carries the vertical, longitudinal, and lateral loads.

During pure longitudinal slip of the rolling tire, the contact area is partitioned into a slip zone and an adhesion zone [21]. The location of the slip point is critical for delineating the slip zone and the adhesion zone. Moreover, the slip points vary with different slip rates, influencing the longitudinal force's magnitude within the contact area, as shown in Fig. 18.

When there is a relative slip between the tire and the road contact area, the friction between the tire and the ground is dynamic. In such cases, the longitudinal force can be calculated by taking the integral of the vertical load of the bristles and the friction coefficient. This is shown in Eq. (13):

$$F_{sl} = a \int_{u_c}^1 u_s q_z(u) du, \quad (13)$$

where a is half the length of the tire contact area; u_c is the slip point; u_s is the friction coefficient; $q_z(u)$ is a function for arbitrary pressure distribution in the tire contact area.

When there is no relative slip between the tire and the road surface, the longitudinal force at each point of the tread in the adhesion zone is the product of the longitudinal stiffness and the longitudinal deformation of the tread, expressed as:

$$q_x(u) = k_{tx} \Delta x = \frac{k_{tx} S_x}{1 + S_x} au. \quad (14)$$

where k_{tx} is the longitudinal stiffness of the element bristles. Our research group has identified the stiffness of 205/55R16 radial tires [22], and the longitudinal stiffness of the tire selected in this article is 3680000 N/m². The normalized coordinate of the tire contact area is defined with symbol u ; through integration, the longitudinal force expression of the grounding imprinting adhesion area can be obtained as:

$$F_{ad} = a \int_{-1}^{u_c} \frac{k_{tx} S_x}{1 + S_x} au du. \quad (15)$$

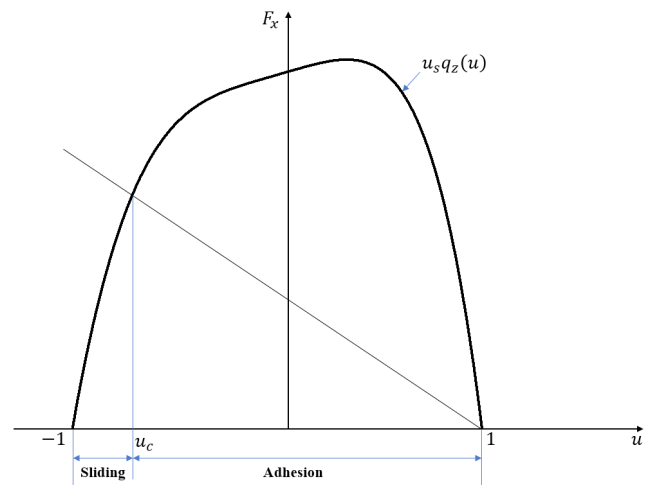


Fig. 18. Slip zone and adhesion zone in the contact area

The slip point is the demarcation point between the adhesion and slip zones. At the slip point, the longitudinal forces in the adhesion and slip zones are equal. Therefore, the joint Eqs. (13) and (15) will lead to Eq. (16).

$$\frac{k_{tx} S_x}{1 + S_x} au_c = u_s q_z(u_c). \quad (16)$$

Upon inputting known parameters into Eq. (16) and utilizing MATLAB software to solve the calculation, the expression is further articulated as:

$$u_c = AF_z u_s (Bz_i^5 - z_i^4 - Bz_i - 1) - 2 \frac{k_{rx} S_x}{1 + S_x} z_i, \quad (17)$$

where z_i ($i=1,2,3,4,5$) results in the equation having a total of 5 roots.

By analyzing Eq. (17) for the slip point u_c , it can be concluded that the slip rate, load, and longitudinal stiffness directly affect the calculation results of the slip point u_c . Meanwhile, since Eq. (17) for the slip point u_c is a complex equation with 5 roots, the process of solving is too cumbersome, and sometimes judgment failure may occur under the condition of small slip rates. Therefore, it is meaningful to simplify the solution process. As shown in Fig. 19, the tire-road adhesion coefficient estimation function designed in this paper for different slip rates is mainly for the tire's braking condition, and the longitudinal stiffness of the tire tread does not change during the vehicle's driving process. Based on the slip point solution in Eq. (17), the conjecture assumes the formula defined in Eq. (18) for calculating the slip point at different slip rates.

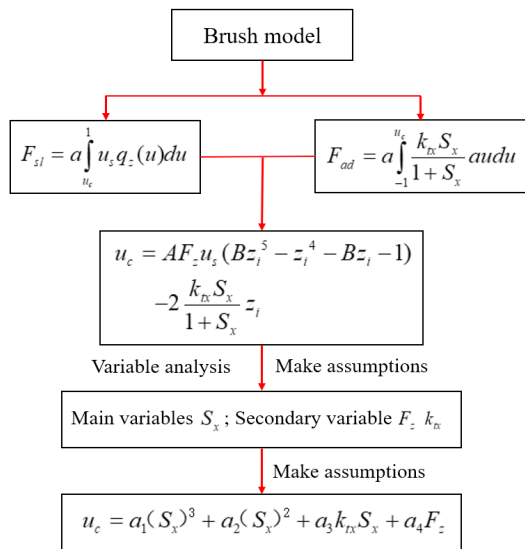


Fig. 19. Variable analysis of the fitting formula

The process of assumption of the fitting formula Eq. (18) is as follows:

1. This paper mainly estimates the tire-road adhesion coefficient under different slip rates, so the slip rate is set as a main variable.
2. According to the analysis of the slip point solution formula in Eq. (17), it is found that tire load and longitudinal stiffness of tread also affect the calculation accuracy of slip point.
3. Tire load and longitudinal stiffness of tread are introduced into the assumption of slip point fitting formula into Eq. (18).
4. Finally, through adjusting the order of the fitting equation function defined in Eq. (18), the slip point fitting function was established and solved.

$$u_c = a_1 (S_x)^3 + a_2 (S_x)^2 + a_3 k_{rx} S_x + a_4 F_z. \quad (18)$$

Figure 20 demonstrates the slip point fitting results for different slip rates at a load of 4000 N with constant longitudinal tire tread stiffness. Equation (18) can be fitted fairly good, which proves that the assumptions made in Eq. (18) in this paper are correct. This article exploits the calculation method to obtain the split point u_c under six load conditions of 2000 N, 2500 N, 3000 N, 3500 N, 4000 N, and 4500 N for data fitting, the slip rate ranges from 0.02 to 0.6 with intervals of 0.02, the friction coefficient is set at 0.5, and the tire's rolling speed is maintained at 19.44 km/h. Table 4 shows the values of a_1, a_2, a_3 and a_4 under six groups of load conditions.

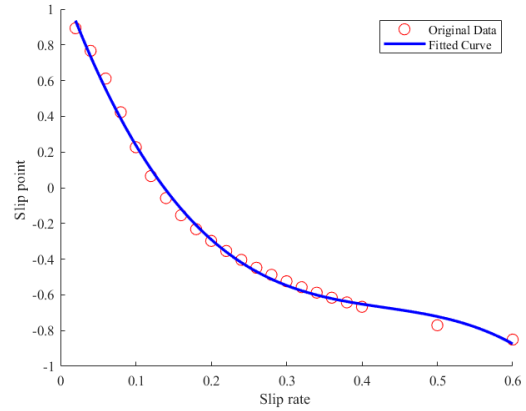


Fig. 20. Data fitting process

From Table 4, it is evident that with the increase in load, the values of fitting coefficients a_1, a_2 and a_3 exhibit a gradual decrease, and the rate of decrease diminishes progressively. The fitting coefficient a_4 undergoes a fluctuating pattern with increasing load, showing a nonlinear relationship. To make the formula of split point u_c respond to the changing trend of tire load, the relationship between a_1, a_2, a_3 and a_4 coefficients and load is analyzed respectively, nonlinear fitting is carried out in the MATLAB fitting toolbox. The fitting relationship between a_1, a_2, a_3 and a_4 and the load is shown in the following equation:

$$\begin{cases} a_1 = p_1 F_z^3 + p_2 F_z^2 + p_3 F_z + p_4 \\ a_2 = p_1 F_z^3 + p_2 F_z^2 + p_3 F_z + p_4 \\ a_3 = p_1 F_z^5 + p_2 F_z^4 + p_3 F_z^3 + p_4 F_z^2 + p_5 F_z + p_6 \\ a_4 = p_1 F_z^5 + p_2 F_z^4 + p_3 F_z^3 + p_4 F_z^2 + p_5 F_z + p_6 \end{cases} \quad (19)$$

Table 4. Fitted values of a_1, a_2, a_3, a_4 under six sets of loads

Load [N]	a_1	a_2	a_3	a_4	RMSE
2000	-177.6	110	-0.000006653	0.0005979	0.02931
2500	84.13	66.7	-0.000005148	0.0005864	0.02986
3000	-55.04	49.68	-0.000004399	0.0005921	0.02685
3500	-30.6	33.89	-0.00000363	0.0005819	0.03029
4000	-19.68	25.36	0.000003129	0.000289	0.0324
4500	-18.63	24.41	0.00000308	0.0006173	0.02453

Table 5 shows the fitting data of a_1, a_2, a_3, a_4 . To further validate the accuracy of the fitted slip point estimation formula, we substituted the estimated slip point into the longitudinal force formula and compared it with the longitudinal force obtained through finite element simulation. Three simulation scenarios were established to simulate the transition of the rolling tire from free rolling to lock up under load conditions of 2800 N, 3800 N, and 4800 N. The inflation pressure was set at 0.21 MPa, and the coefficient of friction was set to 0.5.

Figure 21 presents the tire's estimated and simulated longitudinal forces under three different load conditions. It can be observed that, with the increase in slip rate, the simulated longitudinal force of the tire increases almost linearly, reaching a maximum value around a slip rate of 10 %, after which it remains constant. The load influences the estimated longitudinal force. When the load is 2800 N, the trends of the simulated and estimated longitudinal forces are generally consistent. As the load increases, the estimated longitudinal force rises more slowly in the low-slip region, and the peak shifts to a higher slip rate. In the high-slip region, the estimated longitudinal force aligns closely with the simulated values, indicating that the

Table 5. Fitted values of $p_1, p_2, p_3, p_4, p_5, p_6$

p_1	p_2	p_3	p_4	p_5	p_6	R^2
1.822×10^{-8}	2.158×10^{-4}	0.8604	-1179	/	/	0.9925
-5.586×10^{-9}	7.201×10^{-5}	-0.3165	498.5	/	/	0.9947
-6.392×10^{-21}	9.935×10^{-17}	-6.044×10^{-13}	1.8×10^{-9}	-2.622×10^{-6}	0.001489	0.9999
3.744×10^{-19}	-5.771×10^{-15}	3.489×10^{-11}	-1.035×10^{-7}	1.505×10^{-4}	-0.08527	0.9998

tire’s longitudinal force estimated at the slip point under Coulomb friction is accurate, with virtually no error in the high-slip region.

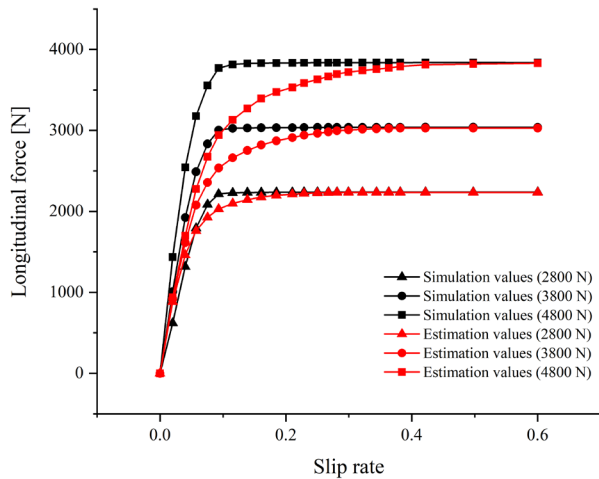


Fig. 21. Longitudinal force estimate and simulation values under the Coulomb friction model

3.3 Tire-road Adhesion Coefficient Estimation

According to the friction theorem, the tire-road adhesion coefficient is defined as the ratio of the longitudinal force and the vertical force of the tire contact area, which is expressed as:

$$\varphi = \frac{F_{ad} + F_{sl}}{F_z} = \frac{a \int_{-1}^{u_s} \frac{k_{tx} S_x}{1 + S_x} a u du + a \int_{u_c}^1 u_s q_z(u) du}{F_z} \quad (20)$$

Given the tire longitudinal stiffness and load one needs to decide upon the appropriate friction model. The friction mechanism between tire rubber and the road surface is complex, involving factors such as the viscoelasticity of the rubber material, road surface roughness, and deformation in the tire contact area. It can be divided into adhesive friction and hysteresis friction [23]. The friction between tire rubber and the road surface is nonlinear, meaning the friction coefficient is not constant. When the slip ratio is low, adhesive friction plays the primary role during braking. As the slip ratio increases, hysteresis friction gradually becomes more prominent. When the slip ratio approaches full slip, the friction force tends to saturate and slightly decrease. Therefore, this paper adopts an exponential decay friction model to describe the nonlinear friction characteristics between tire rubber and the ground, aiming to improve the accuracy of friction force prediction under dynamic conditions, as shown in Eq. (21).

$$u_s = u_k + (u_h - u_k) e^{-\alpha \cdot s} \quad (21)$$

where u_k is the dynamic friction coefficient at the highest slip speed, u_h is the static friction coefficient at zero slip velocity, α is a self-defined attenuation coefficient according to road roughness, and s is the slip speed.

The static friction coefficient is closely related to the roughness of the road surface, while the decay coefficient is highly dependent

on surface roughness [23]. In [23], the authors compared the friction forces under Coulomb friction and exponential decay friction models for a static friction coefficient of 0.3. By selecting decay coefficient values of 0.05 and 0.5 to represent good and poor surface roughness, respectively, they compared the variation in friction coefficient with sliding speed, as shown in Fig. 22.

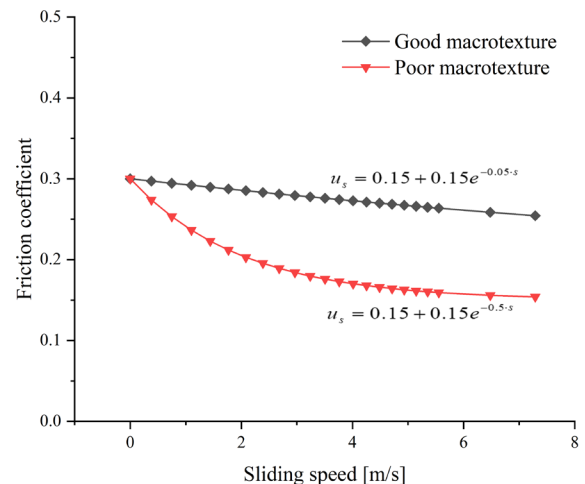


Fig. 22. Slip starting position under different slip rates

To validate the Eq. (20), which incorporates an exponential decay friction model and can accurately estimate the longitudinal force and friction characteristics between tire rubber and road surface, we obtained the optimal slip ratio and peak adhesion coefficient during braking, and provided accurate inputs for active safety control of vehicles. This study used finite element simulation software (Abaqus) to perform simulation analysis of the tire transitioning from free rolling to full slip under three load conditions: 2800 N, 3800 N, and 4800 N. A comparison between the finite element simulation results and the estimates from Eq. (20) is shown in Fig. 23, which illustrates the comparison between the simulated longitudinal force and the estimated longitudinal force obtained using the exponential decay friction model. Using the exponential friction model, the peak longitudinal force changes with the load increase; when the load is 2800 N, 3800 N, and 4800 N, the peak longitudinal force appears near the slip rate of 14 %, 18 %, and 22 %. After that, it began to decline, and the simulation results were consistent with the estimated results.

Based on the simulation results, the feasibility of Eq. (20) in estimating the tire-road adhesion coefficient at different slip rates was verified. The vehicle speed sensor and wheel speed sensor measure the tire’s linear and angular velocities, and the tire’s slip rate is solved according to Eq. (7). Finally, the estimation of the tire-road adhesion coefficient at different slip rates is completed based on the method of estimating the contact area length and the slip point solution method established in Section 2.3 and 3.2. Finally, the tire-road adhesion coefficient under different slip rates can be estimated by inputting

vehicle speed, tire angular velocity, longitudinal stiffness, load, and slip point.

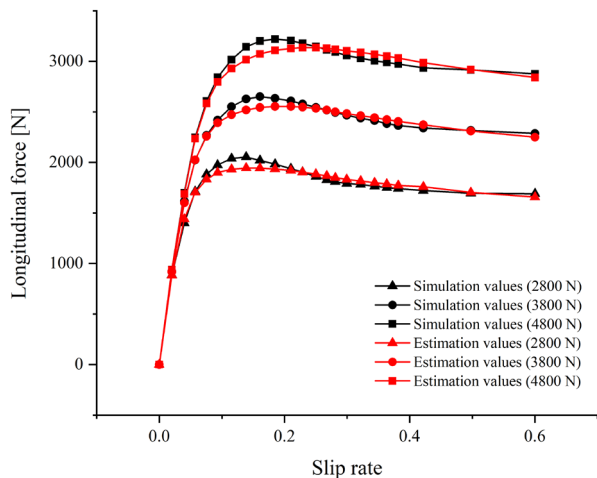


Fig. 23. Longitudinal force estimate and simulation values under the exponential friction model

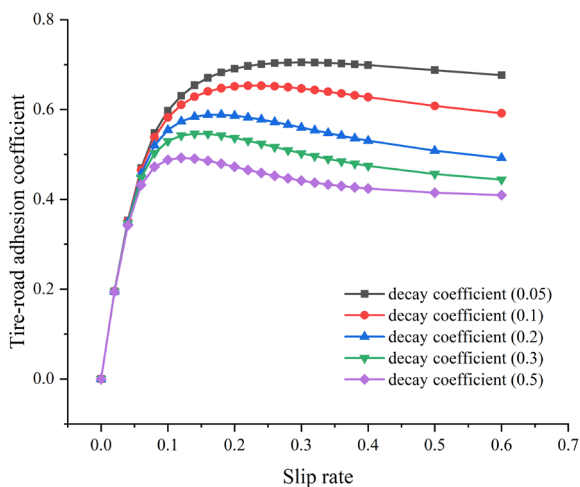


Fig. 24. Estimation results of tire-road adhesion coefficient under different slip rates

Figure 24 shows the estimated values of tire-road adhesion coefficient under different slip rates when the decay coefficient of the exponential decay friction model is 0.05, 0.1, 0.2, 0.3, 0.4, 0.5. It can be obtained that the estimated tire-road adhesion coefficient rises rapidly in an approximately linear relationship before reaching the peak adhesion coefficient when the slip rate is 15 % to 20 %, and then begins to decline slowly. This is due to the local increase of relative slip in the tire contact area before reaching the peak adhesion coefficient, resulting in slower tire-road adhesion coefficient with the increase of slip rate. Because the dynamic friction factor between friction pairs is smaller than the static friction factor, the estimated tire-road adhesion coefficient gradually decreases after reaching the peak adhesion coefficient, consistent with the resulting trend in the references [24,25]. As noted in the previous discussion and based on [26], the decay rate is related to the surface roughness of the road. It can be observed that a higher decay rate results in a lower peak adhesion coefficient between the tire and the road surface, as well as a lower optimal slip rate, which is consistent with [27,28]. Therefore, the tire-road adhesion coefficient estimation under different slip rates designed in this paper can effectively identify the optimal tire slip rates and the vehicle's peak tire-road adhesion coefficients during the driving process. It provides accurate inputs for the whole vehicle's drive anti-skid control and, simultaneously, can improve the control

accuracy of the vehicle's anti-lock braking system (ABS) and other active safety control systems [29].

4 CONCLUSION

This study combines strain sensors with a brush model to develop a method for estimating the tire-road adhesion coefficient of rolling tires at various slip rates during braking. The following conclusions were drawn from this study:

1. During the braking process of rolling tires, the average peak angle spacing between the first-order and second-order curves of the tire's inner layer centerline circumferential strain can effectively represent the tire contact angle, and an estimation method for the contact angle of rolling tires is put forward by using the circumferential strain signal characteristics. Considering the asymmetry of the front and rear contact angles of rolling tires in a braking state, an arc length formula is employed to estimate the rolling tire contact area length; the arc length formula calculates the arc length based on the central angle and radius, with a defined factor aimed at minimizing the discrepancy between the arc length and the straight line. The maximum relative error of the estimated values using the arc length formula compared with the simulation results is less than 3 mm. This method offers an approach for utilizing innovative tires to estimate the contact area length.
2. Considering that the rolling tire contact pressure distribution is affected by conditions such as load, inflation pressure, friction coefficient, etc., an arbitrary pressure distribution function is selected to describe the pressure distribution of the rolling tire during braking. The slip point is the pivotal factor for distinguishing between the adhesion and slip zones. Given the influence of load, tire longitudinal stiffness, and slip rate on the rolling tire slip point, as well as the high-order function of the pressure distribution function, a nonlinear regression equation is used to establish the estimation function for the slip point. The comparison between simulation values and estimated values of longitudinal force confirms the accuracy of the estimation method using the nonlinear regression equation.
3. An estimation method based on the designed contact area length and slip point, employing the brush model, developed a method for estimating tire-road adhesion coefficient. This method establishes the functional relationship between the tire-road adhesion coefficient and the slip rate, determining the required input parameters: slip rate, load, tire longitudinal stiffness, slip point, and contact area length. Assuming a known load, the tire-adhesion coefficient estimation method presented in this paper enables the estimation of the road adhesion coefficient of rolling tires at various slip rates during braking. By integrating sensors and mathematical models, this method offers a technical solution for applying intelligent tires in vehicle control, contributing positively to the future development of intelligent tire technology.
4. Due to the difficulty of controlling the slip rate and measuring the slip point location, this study did not conduct actual vehicle experiments on various road surfaces. The method designed in this paper for estimating the tire-road adhesion coefficient under different slip rates mainly considers the pure longitudinal slip condition of the tire. It does not take into consideration the vehicle's lateral slip, composite conditions during driving, and estimation of parameters such as wheel steering, slip angle, wheel alignment angle, etc., which has some limitations on the prospect of the vehicle's application. In future research work, contact pressure distribution tests of rolling tires, identification and calibration tests of the parameters in the slip point fitting equations, and tests of tire-road adhesion coefficients at different slip rates will be conducted to optimize further the method of tire-road adhesion coefficient estimation established in this paper.

References

- [1] Li, G., Xie, R., Wei, S., Zong C. Estimation of vehicle status and road adhesion coefficient based on dual-volume Kalman filter. *Scie Sinic Technol* 45 403-414 (2015) DOI:10.1360/N092014-00207.
- [2] Wang, Y., Liang, G., Wei Y. Intelligent tire pavement identification algorithm based on support vector machine. *Autom Eng* 42 1671-1678 (2021) DOI:10.19562/j.chinasae.qcgc.2020.12.009.
- [3] Khaleghian, S., Emami, A., Taheri, S. A technical survey on tire-road friction estimation. *Friction* 5 123-146 (2017) DOI:10.1007/s40544-017-0151-0.
- [4] Alonso, J., López, J. M., Pavón, I., Recuero, M., Asensio, C., Arcas, G., et al. On-board wet road surface identification using tyre/road noise and support vector machines. *Appl Acoust* 76 407-415 (2014) DOI:10.1016/j.apacoust.2013.09.011.
- [5] Kongrattanprasert, W., Nomura, H., Kamakura, T., Ueda, K. Detection of road surface states from tire noise using neural network analysis. *IEEJ Trans Indust Applic* 130 920-925 (2010) DOI:10.1541/ieejias.130.920.
- [6] Erdogan, G., Alexander, L., Rajamani, R. Estimation of tire-road friction coefficient using a novel wireless piezoelectric tire sensor. *IEEE Sens J* 11 267-279 (2010) DOI:10.1109/JSEN.2010.2053198.
- [7] Kuno, T., Sugiura, H. Detection of road conditions with CCD cameras mounted on a vehicle. *Syst Comput Jpn*, 30 88-99 (2015) DOI:10.1002/(SICI)1520684X(199912)30:14<88::AID-SCJ9>3.0.CO;2-8.
- [8] Xu, N., Askari, H., Huang, Y., Zhou, J., Khajepour, A. Tire force estimation in intelligent tires using machine learning. *IEEE T Intell Transp* 23 3565-3574 (2020) DOI:10.1109/TITS.2020.3038155.
- [9] Xiong, Y., Yang, X. A review on in-tire sensor systems for tire-road interaction studies. *Sensor Rev* 38 231-238 (2018) DOI:10.1108/SR-07-2017-0132.
- [10] Rajamani, R., Phanomchoeng, G., Piyabongkarn, D., Lew, J.Y. Algorithms for real-time estimation of individual wheel tire-road friction coefficients. *IEEE-ASME T Mech* 17 1183-1195 (2011) DOI:10.1109/TMECH.2011.2159240.
- [11] Matsuzaki, R., Kamai, K., Seki, R. Intelligent tires for identifying coefficient of friction of tire/road contact surfaces using three-axis accelerometer. *Smart Mater Struct* 24 025010 (2014) DOI:10.1088/0964-1726/24/2/025010.
- [12] Rajamani, R., Piyabongkarn, N., Lew, J., Yi, K., Phanomchoeng, G. Tire-road friction-coefficient estimation. *IEEE Contr Syst Mag* 30 54-69 (2010) DOI:10.1109/MCS.2010.937006.
- [13] Nishihara, O., Masahiko, K. Estimation of road friction coefficient based on the brush model. *T Jpn Soc Mech Eng* 75 041006 (2011) DOI:10.1115/1.4003266.
- [14] Zhou, H., Li, H., Yang, J., Chen, Q., Wang, G., Han, T., et al. A strain-based method to estimate longitudinal force for intelligent tires by using a physics-based model. *Stroj Vestn-J Mech E* 67 153-166 (2021) DOI:10.5545/sv-jme.2020.7068.
- [15] Li, B., Quan, Z., Bei, S., Zhang, L., Mao, H. An estimation algorithm for tire wear using intelligent tire concept. *P I Mech Eng D J Aut* 235 2712-2725 (2021) DOI:10.1177/0954407021999483.
- [16] Zhou, H., Li, H., Liang, C., Zhang, L., Wang, G. Relationship between tire ground characteristics and vibration noise. *Stroj Vestn-J Mech E* 67 11-27 (2021) DOI:10.5545/SV-JME.2020.6946.
- [17] Mei, F. *Research on Finite Element Automatic Modeling Technology of Radial Tire Tread Pattern*. PhD Thesis, Shandong University, Shandong (2020).
- [18] Gu, T., Li, B., Quan, Z., Bei, S., Yin, G., Guo, J., et al. The vertical force estimation algorithm based on smart tire technology. *World Electr Vehic J* 13 104 (2022) DOI:10.3390/wevj13060104.
- [19] Romano, L., Sakhnevych, A., Strano, S., Timpone, F. A novel brush-model with flexible carcass for transient interactions. *Meccanica*, 54 1663-1679 (2019) DOI:10.1007/s11012-019-01040-0.
- [20] Guo, K., Lu, D., Chen, S.K., Lin, W.C., Lu, X. P. The UniTire model: a nonlinear and non-steady-state tyre model for vehicle dynamics simulation. *Vehicle Syst Dyn* 43 341-358 (2005) DOI:10.1080/00423110500140690.
- [21] Mavros, G., Rahnejat, H., King, P.D. Transient analysis of tyre friction generation using a brush model with interconnected viscoelastic bristles. *P I Mech Eng K-J Mul* 219 275-283 (2005) DOI:10.1243/146441905X9908.
- [22] Riehm, P., Unrau, H.J., Gauterin, F., Torbrügge, S., Wies, B. 3D brush model to predict longitudinal tyre characteristics. *Vehicle Syst Dyn* 57 17-43 (2019) DOI:10.1080/00423114.2018.1447135.
- [23] Wang, H., Al-Qadi, I.L., Stanciulescu, I. Effect of surface friction on tire-pavement contact stresses during vehicle maneuvering. *J Eng Mech* 140 04014001 (2014) DOI:10.1061/(ASCE)EM.1943-7889.0000691.
- [24] Rajendran, S., Spurgeon, S.K., Tsampardoukas, G., Hampson, R. Estimation of road frictional force and wheel slip for effective antilock braking system (ABS) control. *Int J Robust Nonlin* 29 736-765 (2019) DOI:10.1002/mc.4366.
- [25] Han, T. *Research on Intelligent Tire Vertical/Longitudinal Force Estimation Algorithm Based on Flexible Ring Model*. PhD Thesis, Jiangsu University, Zhenjiang (2020)
- [26] Gustafsson, F. Slip-based tire-road friction estimation. *Automatica* 33 1087-1099 (1997) DOI:10.1016/S0005-1098(97)00003-4.
- [27] Yu, M., Wu, G., Kong, L., Tang, Y. Tire-pavement friction characteristics with elastic properties of asphalt pavements. *Appl Sci-Basel* 7 1123 (2017) DOI:10.3390/app711123.
- [28] Gerthoffert, J., Cerezo, V., Thiery, M., Bouteldja, M., Do, M.T. A brush-based approach for modelling runway friction assessment device. *Int J Pavement En* 21 1694-1702 (2020) DOI:10.1080/10298436.2018.1563786.
- [29] Sheng, S.G. *Research on Stability Control of Distributed Drive Pure Electric Vehicle Based on Tyre Force Observation*, MSc Thesis Jilin University, Jilin (2023)

Acknowledgements This study was financially supported by the National Natural Science Foundation of China (52072156,52272366) and the Postdoctoral Foundation of China (2020M682269).

Received 2024-05-12, **revised:** 2024-11-13, 2025-01-06, 2025-02-07, **accepted:** 2025-04-01.

Author Contribution Jintao Zhang: writing – original draft, visualization, validation, methodology. Zhecheng Jing: investigation, resources, conceptualization, data curation. Haichao Zhou: writing – original draft, methodology, investigation, conceptualization. Yu Zhang: conceptualization. Guolin Wang: validation, supervision, conceptualization.

Data Availability The data supporting the findings of this study are included in the article.

Metoda določanja koeficienta oprijema med pnevmatiko in cestiščem na podlagi fizikalnega modela pnevmatike in deformacijskega signala pri čistem vzdolžnem zdrsu

Povzetek Za natančen izračun koeficienta oprijema med kotalno pnevmatiko in cestiščem pri različnih stopnjah zdrsa ter izboljšanje varnosti in stabilnosti vozila je bila predlagana metoda ocene koeficienta oprijema med pnevmatiko in cestiščem, ki temelji na deformacijskih senzorjih in ščetkastih (brush) modelih. Najprej je bil izdelan FEM model radialne pnevmatike dimenzij 205/55R16, katerega učinkovitost je bila potrjena s poskusi statičnega stika s podlago in merjenjem radialne togosti. Nato je bil med zaviranjem pridobljen signal obodne deformacije vzdolž sredinske linije notranje površine pnevmatike, dolžina kontaktne površine pa je bila ocenjena z uporabo formule za dolžino loka na podlagi povprečne razdalje med vrhovi prvega in drugega reda krivulj obodne deformacije. Simulacija zaviranja kotalnih pnevmatik je potrdila nesimetričnost porazdelitve tlaka na kontaktni površini. Položaj točke zdrsa znotraj kontaktne površine je bil ocenjen na podlagi poljubne funkcije porazdelitve tlaka in ščetkastega modela. Za določitev ocenjevalne funkcije točke zdrsa pri različnih stopnjah zdrsa je bila uporabljena nelinearna regresija. Vzpostavljena je bila funkcionalna zveza med koeficientom oprijema pnevmatika-cestišče in stopnjo zdrsa, ki upošteva značilnosti trenja med gumijasto površino pnevmatike in cestiščem, pri čemer je bil uporabljen model trenja na osnovi eksponentnega upadanja. Rezultati kažejo, da opisana metoda omogoča oceno koeficienta oprijema med pnevmatiko in cestiščem pri različnih stopnjah zdrsa, kar zagotavlja dragoceno spoznanja za aplikacije inteligentnih pnevmatik na področju nadzora dinamike vozil.

Ključne besede inteligentna pnevmatika, ocena koeficienta oprijema med pnevmatiko in cestiščem, točka zdrsa, stopnja zdrsa, nelinearna regresija